



Has JWST Already Falsified Dark-matter-driven Galaxy Formation?

Moritz Haslbauer^{1,2}, Pavel Kroupa^{1,3}, Akram Hasani Zonoozi⁴, and Hosein Haghi⁴¹ Helmholtz-Institut für Strahlen- und Kernphysik (HISKP), University of Bonn, Nussallee 14–16, D-53115 Bonn, Germany; mhaslbauer@astro.uni-bonn.de² Max-Planck-Institut für Radioastronomie, Auf dem Hügel 69, D-53121 Bonn, Germany³ Astronomical Institute, Faculty of Mathematics and Physics, Charles University, V Holešovičkách 2, CZ-180 00 Praha 8, Czech Republic⁴ Department of Physics, Institute for Advanced Studies in Basic Sciences (IASBS), Zanjan 45137-66731, Iran

Received 2022 July 28; revised 2022 October 13; accepted 2022 October 13; published 2022 November 10

Abstract

The James Webb Space Telescope (JWST) discovered several luminous high-redshift galaxy candidates with stellar masses of $M_* \gtrsim 10^9 M_\odot$ at photometric redshifts $z_{\text{phot}} \gtrsim 10$, which allows to constrain galaxy and structure formation models. For example, Adams et al. identified the candidate ID 1514 with $\log_{10}(M_*/M_\odot) = 9.8^{+0.2}_{-0.2}$ located at $z_{\text{phot}} = 9.85^{+0.18}_{-0.12}$ and Naidu et al. found even more distant candidates labeled as GL-z11 and GL-z13 with $\log_{10}(M_*/M_\odot) = 9.4^{+0.3}_{-0.3}$ at $z_{\text{phot}} = 10.9^{+0.5}_{-0.4}$ and $\log_{10}(M_*/M_\odot) = 9.0^{+0.3}_{-0.4}$ at $z_{\text{phot}} = 13.1^{+0.8}_{-0.7}$, respectively. Assessing the computations of the IllustrisTNG (TNG50-1 and TNG100-1) and EAGLE projects, we investigate if the stellar mass buildup as predicted by the Λ CDM paradigm is consistent with these observations assuming that the early JWST calibration is correct and that the candidates are indeed located at $z \gtrsim 10$. Galaxies formed in the Λ CDM paradigm are by more than an order of magnitude less massive in stars than the observed galaxy candidates implying that the stellar mass buildup is more efficient in the early universe than predicted by the Λ CDM models. This in turn would suggest that structure formation is more enhanced at $z \gtrsim 10$ than predicted by the Λ CDM framework. We show that different star formation histories could reduce the stellar masses of the galaxy candidates alleviating the tension. Finally, we calculate the galaxy-wide initial mass function (gwIMF) of the galaxy candidates assuming the integrated galaxy IMF theory. The gwIMF becomes top-heavy for metal-poor star-forming galaxies decreasing therewith the stellar masses compared to an invariant canonical IMF.

Unified Astronomy Thesaurus concepts: Cold dark matter (265); Initial mass function (796); Stellar mass functions (1612); Stellar masses (1614); Galaxy evolution (594); Galaxy formation (595); Galaxy mass distribution (606); Galaxy properties (615); High-redshift galaxies (734); Early universe (435); Cosmology (343); James Webb Space Telescope (2291)

1. Introduction

The formation of the first galaxies in the observed universe is a key question in modern astrophysics and one of the most important science goals of the recently launched James Webb Space Telescope (JWST). The Near Infrared Camera instrument (NIRCam; Rieke et al. 2005) of JWST observes the universe in the $\approx 0.6\text{--}5 \mu\text{m}$ regime. This allows the detection of objects at redshifts $z \gtrsim 12$, thus, revealing the evolutionary stage of galaxies in the early universe just ≈ 400 Myr after the Big Bang. The most distant confirmed galaxy is GN-z11 with a stellar mass of $M_* \approx 10^9 M_\odot$ at a spectroscopic redshift of $z_{\text{spec}} = 11.09^{+0.08}_{-0.12}$ detected with the Hubble Space Telescope (Oesch et al. 2016). Recently, Naidu et al. (2022b) reported the discovery of two luminous galaxy candidates labeled as GLASS-z11 (hereafter GL-z11) and GLASS-z13 (GL-z13) with $\log_{10}(M_*/M_\odot) = 9.4^{+0.3}_{-0.3}$ and $9.0^{+0.3}_{-0.4}$ located at photometric redshifts of $z_{\text{phot}} = 10.9^{+0.5}_{-0.4}$ and $z_{\text{phot}} = 13.1^{+0.8}_{-0.7}$, respectively (see their Table 3). In a subsequent publication, Naidu et al. (2022a) presented the galaxy candidate CEERS-1749 with $\log_{10}(M_*/M_\odot) = 9.6^{+0.2}_{-0.2}$ most likely located at $z_{\text{phot}} = 16.0^{+0.6}_{-0.6}$ but a secondary redshift solution of $z \approx 5$ cannot be excluded (see their Figure 1 and Table 3).

Further luminous high-redshift galaxy candidates have been discovered by JWST (e.g., Adams et al. 2022; Atek et al. 2022; Furtak et al. 2022; Harikane et al. 2022; Yan et al. 2022; Labbe et al. 2022). For example, Adams et al. (2022) studied the properties of candidates over a redshift range of $9 < z_{\text{phot}} < 12$ and the source with ID 1514 has $\log_{10}(M_*/M_\odot) = 9.8^{+0.2}_{-0.2}$ at $z_{\text{phot}} = 9.85^{+0.18}_{-0.12}$ (see their Tables 3 and 5). Labbe et al. (2022) identified candidates with $M_* > 10^{10} M_\odot$ over $7 < z_{\text{phot}} < 11$ from which the two most massive are ID 14924 with $\log_{10}(M_*/M_\odot) = 10.93$ at $z_{\text{phot}} = 9.92$ and ID 38094 with $\log_{10}(M_*/M_\odot) = 11.16$ at $z_{\text{phot}} = 7.56$ (see their Figure 3). The spectroscopical confirmation of these objects is still outstanding because the high photometric redshifts of these galaxy candidates can, e.g., artificially emerge due to dust attenuation (Naidu et al. 2022a, 2022b; Zavala et al. 2022).

In this contribution, we aim to investigate if ID 1514, ID 14924, GL-z11, GL-z13, and CEERS-1749 are consistent with the hierarchical buildup of stellar mass as predicted by the Λ CDM paradigm (Efstathiou et al. 1990; Ostriker & Steinhardt 1995) using the Illustris The Next Generation (TNG; Pillepich et al. 2018a; Nelson et al. 2019b; Pillepich et al. 2019) and Evolution and Assembly of Galaxies and their Environments (EAGLE; Crain et al. 2015; Schaye et al. 2015; McAlpine et al. 2016) projects.

2. Method

The IllustrisTNG (Pillepich et al. 2018a, 2018b; Marinacci et al. 2018; Naiman et al. 2018; Nelson et al. 2018, 2019a, 2019b;



Original content from this work may be used under the terms of the [Creative Commons Attribution 4.0 licence](https://creativecommons.org/licenses/by/4.0/). Any further distribution of this work must maintain attribution to the author(s) and the title of the work, journal citation and DOI.

Springel et al. 2018; Pillepich et al. 2019) and EAGLE (Crain et al. 2015; Schaye et al. 2015; McAlpine et al. 2016) projects consist of a suite of hydrodynamical cosmological simulation runs conducted in the Λ CDM framework.

The IllustrisTNG project assumes a Planck-2015 (Planck Collaboration XIII 2016) cosmology with the cosmological parameters being $H_0 = 67.74 \text{ km s}^{-1} \text{ Mpc}^{-1}$, $\Omega_{b,0} = 0.0486$, $\Omega_{m,0} = 0.3089$, $\Omega_{\Lambda,0} = 0.6911$, $\sigma_8 = 0.8159$, and $n_s = 0.9667$. The simulation runs are based on the moving-mesh code AREPO (Springel 2010) and self-consistently evolve the gas cells, stellar, black hole, and dark matter particles from redshift $z = 127$ up to present time. The Subfind Subhalos⁵ and Group⁶ catalogs are available for 100 different time steps (snapshots) in the redshift range of $0 \leq z \leq 20.05$. Here, we analyze the snapshot at redshift $z = 14.99$ (corresponding to an age of the universe of $t = 0.271 \text{ Gyr}$ and a snapshot number of $\text{snapnum} = 1$), at $z = 11.98$ ($t = 0.370 \text{ Gyr}$, $\text{snapnum} = 2$), at $z = 10.98$ ($t = 0.418 \text{ Gyr}$, $\text{snapnum} = 3$), and at $z = 10.00$ ($t = 0.475 \text{ Gyr}$, $\text{snapnum} = 4$) of the high-resolution realization TNG50-1 and TNG100-1. The former has a box side of $35 h^{-1} = 51.7 \text{ comoving Mpc (cMpc)}$, respectively, where h is the present Hubble constant H_0 in units of $100 \text{ km s}^{-1} \text{ Mpc}^{-1}$, a baryonic element mass of $m_b = 8.5 \times 10^4 M_\odot$, and a dark matter particle mass of $m_{\text{dm}} = 4.5 \times 10^5 M_\odot$. TNG100-1 has, with $75 h^{-1} = 110.7 \text{ cMpc}$, a larger box size and with $m_b = 1.4 \times 10^6 M_\odot$, and $m_{\text{dm}} = 7.5 \times 10^6 M_\odot$, a lower resolution than TNG50-1 (see, e.g., also Table 1 of Nelson et al. 2019b).

The EAGLE project is consistent with the Planck-2013 (Planck Collaboration I 2014) cosmology being $H_0 = 67.77 \text{ km s}^{-1} \text{ Mpc}^{-1}$, $\Omega_{b,0} = 0.04825$, $\Omega_{m,0} = 0.307$, $\Omega_{\Lambda,0} = 0.693$, $\sigma_8 = 0.8288$, and $n_s = 0.9611$ (see also Table 1 of Schaye et al. 2015). Its simulations run with a modification of the GADGET-3 smoothed particle hydrodynamics code (e.g., Springel 2005) starting also at $z = 127$ and self-consistently evolving the baryonic and dark matter particles up to the present day. The publicly available subhalo catalogs (Table B.1 of McAlpine et al. 2016) are recorded for 29 snapshots in the redshift range of $0 \leq z \leq 20.00$ (see Table C.1 of McAlpine et al. 2016). We use the two high-resolution realization runs RefL0025N0752 and RecalL0025N0752, and the two lower resolution runs RefL0050N0752 and RefL0100N1504 at $z = 15.13$ ($\text{snapnum} = 1$) and $z = 9.99$ ($\text{snapnum} = 2$). The two high-resolution runs have a box size of 25 cMpc with an initial baryonic particle mass of $m_b = 2.26 \times 10^5 M_\odot$, and a dark matter particle mass of $m_{\text{dm}} = 1.21 \times 10^6 M_\odot$. RefL0050N0752 and RefL0100N1504 have a size of 50 cMpc and 100 cMpc , respectively, and both have an initial baryonic particle mass of $m_b = 1.81 \times 10^6 M_\odot$ and a dark matter particle mass of $m_{\text{dm}} = 9.70 \times 10^6 M_\odot$ (Table 2 of Schaye et al. 2015).

3. Results

The galaxy stellar mass function (GSMF) at redshifts $z = 14.99$, 11.98 , 10.98 , and 10.00 in the TNG runs and at $z = 15.13$ and 9.99 in the EAGLE runs are presented in Figure 1. The global peak of the distribution depends on the resolution and/or box size of the simulation runs such that the formation of low massive galaxies depends on the particle resolution but also because small simulation boxes lack

large-scale density fluctuations. As a consequence, not-large-enough simulation boxes would not allow the formation of large galaxy clusters, therefore hampering the growth of central (but also noncentral) galaxies. Thus, we mainly focus on the larger simulation boxes TNG100-1 and RefL0100N1504.

In the following, we compare the stellar mass buildup as predicted by the Λ CDM simulations with the masses of the observed high-redshift galaxy candidates ID 1514 (Adams et al. 2022), ID 14924 (Labbe et al. 2022)⁷, GL-z11, GL-z13 (Naidu et al. 2022b), and CEERS-1749 (Naidu et al. 2022a). For the TNG runs, ID 1514 located at $z_{\text{phot}} = 9.85^{+0.18}_{-0.12}$ and ID 14924 at $z_{\text{phot}} = 9.92$ are compared with simulated galaxies at $z = 10.00$. GL-z11 at $10.9^{+0.5}_{-0.4}$, GL-z13 at $13.1^{+0.8}_{-0.7}$, and CEERS-1749 at $16.0^{+0.6}_{-0.6}$ are compared with the simulations at $z = 10.98$, 11.98 , and 14.99 , respectively. The comparison with GL-z13 and CEERS-1749 is therewith more conservative because snapshots corresponding to lower redshifts than observed are addressed allowing the galaxies to grow in stars for a longer time span than in the observed cases.

In TNG100-1, the GSMF at $z = 14.99$ reaches a maximum value of $\log_{10}(M_*/M_\odot) = 7.32$ being therewith ≈ 191 times lower than the stellar mass of CEERS-1749 with $\log_{10}(M_*/M_\odot) = 9.6^{+0.2}_{-0.2}$. At $z = 11.98$ and $z = 10.98$, the maximum stellar masses of subhalos are $\log_{10}(M_*/M_\odot) = 8.07$ and 8.43 , respectively, which is less massive than GL-z13 with $\log_{10}(M_*/M_\odot) = 9.0^{+0.3}_{-0.4}$ and GL-z11 with $\log_{10}(M_*/M_\odot) = 9.4^{+0.3}_{-0.3}$. The maximum value of $\log_{10}(M_*/M_\odot) = 8.73$ at $z = 10.00$ is significantly lower than the stellar mass of ID 1514, which has $\log_{10}(M_*/M_\odot) = 9.8^{+0.2}_{-0.2}$. The discrepancy becomes even more significant for ID 14924, which has $\log_{10}(M_*/M_\odot) = 10.93$ at $z_{\text{phot}} = 9.92$. The above stellar masses refer to all stellar particles bound to the considered subhalo depending therewith on the subhalo-finding algorithm. The identification of subhalos can be disturbed, e.g., by merger events, which frequently occur especially at high redshifts. Therefore, we also assess the maximum stellar masses of halos, which accounts for both the fact that the subhalo finder can split a galaxy in clumps underestimating the total mass of the galaxy, and for the inclusion of observationally unresolved satellite galaxies. The maximum stellar masses of halos are $\log_{10}(M_*/M_\odot) = 7.32$ (7.05), 8.10 (7.88), 8.43 (8.24), and 8.78 (8.59) at $z = 14.99$, 11.98 , 10.98 , and 10.00 , in the TNG100-1 (TNG50-1) run, respectively. Thus, using the most massive halo instead of the most massive subhalo in terms of its stellar mass does not significantly effect the results of the TNG runs.

In the EAGLE runs, ID 1514/ID 14924 and CEERS-1749 are compared with the GSMF at $z = 9.99$ and 15.13 , respectively. Unfortunately, the EAGLE database does not list snapshots that match the observed redshifts of GL-z11 and GL-z13. Thus, the EAGLE analysis only focuses on ID 1514, ID 14924, and CEERS-1749.

The RefL0050N0752 and RefL0100N1504 snapshots contain galaxies reaching up to $\log_{10}(M_*/M_\odot) \approx 7.70$ at $z = 15.13$ and $\log_{10}(M_*/M_\odot) \approx 9.06$ at $z = 9.99$, which is ≈ 79 and ≈ 5.5 times lower than the observed stellar mass of CEERS-1749 and ID 1514, respectively. The stellar mass of ID 14924 is 74 times higher than the most massive simulated galaxy at $z = 9.99$.

The evolution of the stellar mass growth is summarized in Figure 2 and Table 1 by showing the maximum stellar mass of a subhalo in dependence of redshift for different simulation runs.

⁵ <https://www.tng-project.org/data/docs/specifications/#sec2b> (23.07.2022).

⁶ <https://www.tng-project.org/data/docs/specifications/#sec2a> (12.09.2022).

⁷ We only show ID 1514 and not the more massive candidate ID 14924 in the bottom right panel of Figure 1 in order to be more conservative.

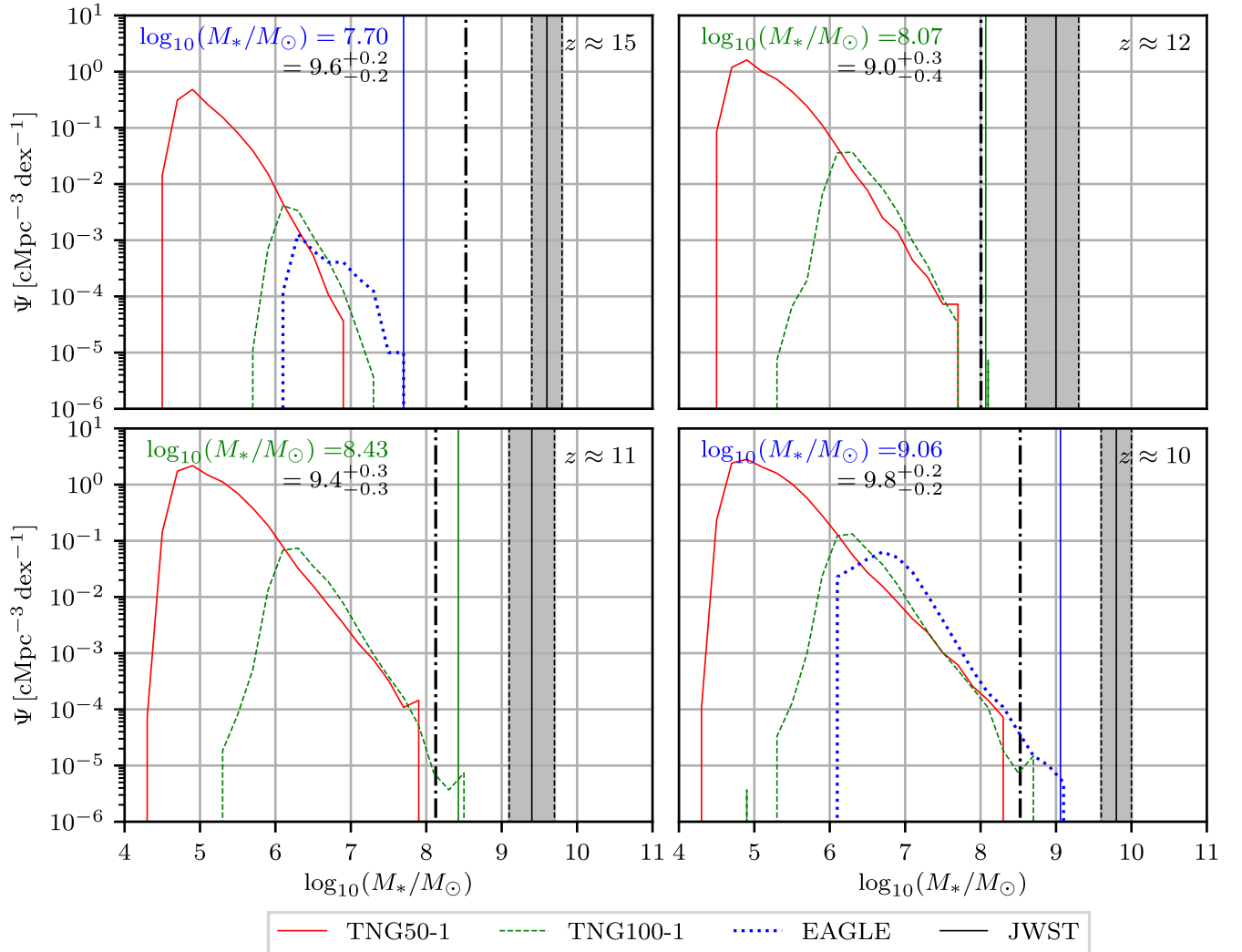


Figure 1. The GSMF at redshifts $z \approx 15$ (top left), 12 (top right), 11 (bottom left), 10 (bottom right) in the TNG50-1 (solid red), TNG100-1 (dashed green), and RefL0100N1504 (dotted blue) simulation. The colored vertical solid line marks the most massive subhalo in terms of the stellar mass in the simulations. The vertical black solid lines refer to the reported galaxy candidates CEERS-1749 (top left), GL-z13 (top right), GL-z11 (bottom left), and ID 1514 (bottom right), where the black dashed lines correspond to the measurement uncertainties. The vertical dashed-dotted lines mark the lowest possible value as inferred for different star formation histories (SFHs) in Section 3.1. The histograms are normalized by their bin width of $\Delta \log_{10}(M_*/M_\odot) = 0.2$ and volume of the simulation box.

The observed high-redshift galaxy candidates are, by more than 1 order of magnitude, more massive than the most massive simulated galaxies in the Λ CDM framework.

The inferred stellar mass of observed galaxies is sensitive to the adopted SFH and initial mass function (IMF). In the following sections, we first investigate if the tension reported here of the stellar mass buildup in the early universe can be resolved if different SFHs of the observed galaxy candidates are assumed. Second, the effect of a varying IMF on the observed stellar masses is discussed.

3.1. The Minimum Inferred Galaxy Masses for Different Star Formation Histories

In order to calculate the minimum possible mass that the observed high-redshift galaxy candidates CEERS-1749, GL-z11, GL-z13, and ID 1514 can have for an invariant IMF, different sets of models of galaxies with different star formation histories (SFHs) are constructed. Using stellar population synthesis models, we let the age of the modeled galaxies vary in the range of $[\approx 4, 400 \text{ Myr}]$ to investigate their UV-band

(1500 Å) stellar mass (including remnants)-to-light ratio, M_*/L_{UV} , for an invariant canonical IMF (Kroupa 2001; Kroupa et al. 2013). The lower limit is set by the implemented stellar evolution tracks of the Padova group (Marigo & Girardi 2007; Marigo et al. 2008; see also Zonoozi et al. 2019) and is roughly comparable to the mean stellar age ($\approx 1\text{--}20 \text{ Myr}$) of observed high-redshift galaxies ($5 \lesssim z_{\text{spec}} \lesssim 8$) as found by Carnall et al. (2022).

Since the spectral energy distribution fitting analysis of high-redshift star-forming galaxies shows more consistency with increasing SFHs, here we adopt the delayed- τ model (e.g., Kroupa et al. 2020a)

$$\psi_{\text{del}}(t) = \psi_0 t \exp(-t/\tau), \quad (1)$$

and an exponentially increasing SFH

$$\psi_{\text{exp}}(t) = \psi_0 \exp(t/\tau), \quad (2)$$

where $\psi(t)$ is the star formation rate (SFR), t is the age since star formation started, ψ_0 is the normalization parameter, and τ is the e-folding timescale. The mass and light of a galaxy are calculated by an integral over the SFR. Note that, using the

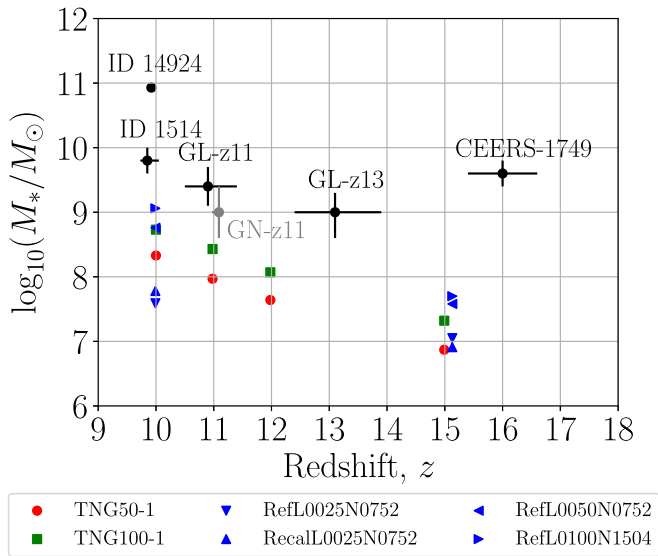


Figure 2. The most massive subhalo in terms of the stellar mass in dependence of redshift in the TNG50-1 (red), TNG100-1 (green), and EAGLE (blue) runs. The black error bars are the observed galaxy candidates by JWST as listed in Table 1. The grey error bar shows GN-z11 (Oesch et al. 2016).

Table 1

Comparison of Several Observed Galaxy Candidates with Λ CDM Simulations

	Redshift (z)	Stellar Mass $\log_{10}(M_*/M_\odot)$
CEERS-1749	$16.0^{+0.6}_{-0.6}$	$9.6^{+0.2}_{-0.2}$ (8.53) ^a
GL-z13	$13.1^{+0.8}_{-0.7}$	$9.0^{+0.3}_{-0.4}$ (8.01) ^a
GL-z11	$10.9^{+0.5}_{-0.4}$	$9.4^{+0.3}_{-0.3}$ (8.13) ^a
ID 1514	$9.85^{+0.18}_{-0.12}$	$9.8^{+0.2}_{-0.2}$ (8.53) ^a
TNG50-1	14.99	6.87
TNG50-1	11.98	7.64
TNG50-1	10.98	7.97
TNG50-1	10.00	8.33
TNG100-1	14.99	7.32
TNG100-1	11.98	8.07
TNG100-1	10.98	8.43
TNG100-1	10.00	8.73
RefL0025N0752	15.13	7.05
RefL0025N0752	9.99	7.59
RecalL0025N0752	15.13	6.91
RecalL0025N0752	9.99	7.78
RefL0050N0752	15.13	7.58
RefL0050N0752	9.99	8.76
RefL0100N1504	15.13	7.70
RefL0100N1504	9.99	9.06

Notes. The first four rows show the photometric redshifts and stellar masses of the observed galaxy candidates ID 1514 (see Tables 3 and 5 of Adams et al. 2022), GL-z11, GL-z13 (see Table 3 of Naidu et al. 2022b), and CEERS-1749 (see Table 3 of Naidu et al. 2022a). The other rows list the maximum stellar mass of a subhalo at a given redshift for the TNG and EAGLE runs.

^a Lowest possible stellar mass value for an invariant canonical IMF as quantified in Section 3.1.

invariant IMF, at a given t , the mass-to-light ratio is independent of the total mass that is converted into stars. This is because of cancellation of the normalization parameter, ψ_0 .

The effect of the SFHs on the M_*/L_{UV} ratio of galaxies by adopting different values of τ is shown in the left panels of Figure 3. We set that galaxies start forming stars 200 Myr after the

Big Bang, with an averaged metallicity of $[\text{Fe}/\text{H}] = -2$, and we assume that the mass loss from galaxies is only through stellar evolution in the form of ejected gas. Since the stellar loss due to dynamical evolution is significant only for systems with initial stellar mass less than $M_* = 10^6 M_\odot$, no stars are lost by the dynamical evolution of galaxies. As can be seen, the minimum mass-to-light ratio that can be considered for these galaxies assuming different SFHs is $M_*/L_{UV} \approx 3.2 \times 10^{-8} M_\odot/L_\odot$.

According to the estimated UV absolute magnitude of these objects, $M_{UV, \text{CEERS-1749}} = -22.0$, $M_{UV, \text{GL-z13}} = -20.7$, $M_{UV, \text{GL-z11}} = -21.0$, and $M_{UV, \text{ID 1514}} = -22.0$ mag, we obtain the lowest possible stellar masses of $\log_{10}(M_*/M_\odot) = 8.53, 8.01, 8.13$, and 8.53 for CEERS-1749, GL-z13, GL-z11, and ID 1514 in the case of an exponential SFH, respectively, as visualized in the right panels of Figure 3.

These lower stellar mass limits just resolve the discrepancy for GL-z11, GL-z13, and ID 1514 (see the vertical dashed-dotted lines in Figure 1). In the case of CEERS-1749, the maximum stellar mass obtained in the Λ CDM simulation is ≈ 6.8 lower than its inferred lower limit.

3.2. Galaxy Masses for a Varying IMF

In the previous section we applied an invariant IMF but recent observations (e.g., Schneider et al. 2018; Zhang et al. 2018; Senchyna et al. 2021) suggest that the mass distribution of a stellar population may depend on its local star-forming environment. Especially metal-poor Population III stars are expected to follow a top-heavy IMF.

A theoretical framework to describe the stellar population of an entire galaxy is the integrated galactic initial mass function (IGIMF) theory, which adds up all the IMFs of star-forming regions (embedded clusters) within a galaxy (Kroupa & Weidner 2003; Weidner & Kroupa 2006). The resulting galaxy-wide IMF (gwIMF) systematically varies with the global SFR and averaged metallicity of the galaxy, i.e., the gwIMF becomes top-heavy for galaxies with $\text{SFR} \gtrsim 1 M_\odot \text{yr}^{-1}$ and metallicities $[\text{Fe}/\text{H}] < 0$ (see Figure 2 of Jeřábková et al. 2018) compared to the canonical IMF. In order to study the effect of a varying IMF on the high-redshift galaxy candidates, we calculate the stellar population of galaxies assuming the latest IGIMF formalism by Yan et al. (2021) and using an IGIMF Fortran code developed by Akram Hasani Zonoozi. For simplification, we assume that all galaxies start to form stars 200 Myr after the Big Bang, with a constant SFR over time, and an average metallicity of $[\text{Fe}/\text{H}] = -2$. Since the gwIMF is time dependent, we require that realistic IGIMF models have to match the observed M_{UV} within ± 1 mag in the 1σ interval of the observed redshift of the corresponding galaxy candidate. The left panel of Figure 4 shows the time evolution of the absolute UV-band magnitude for IGIMF models that fulfill these constraints for observed galaxy candidates CEERS-1749, GL-z13, GL-z11, and ID 1514. These models have constant SFRs in the range of $\approx 2\text{--}30 M_\odot \text{yr}^{-1}$ and thus a top-heavy IMF. The stellar masses at the observed redshifts of the galaxy candidates are shown in the right panel of Figure 4 and are systematically lower than the derived stellar masses of Adams et al. (2022), Naidu et al. (2022b), and Naidu et al. (2022a) because of the top-heavy gwIMF compared to the canonical IMF.

4. Discussion and Conclusion

While the redshifts of the galaxy candidates need to be spectroscopically verified, we use these JWST observations to

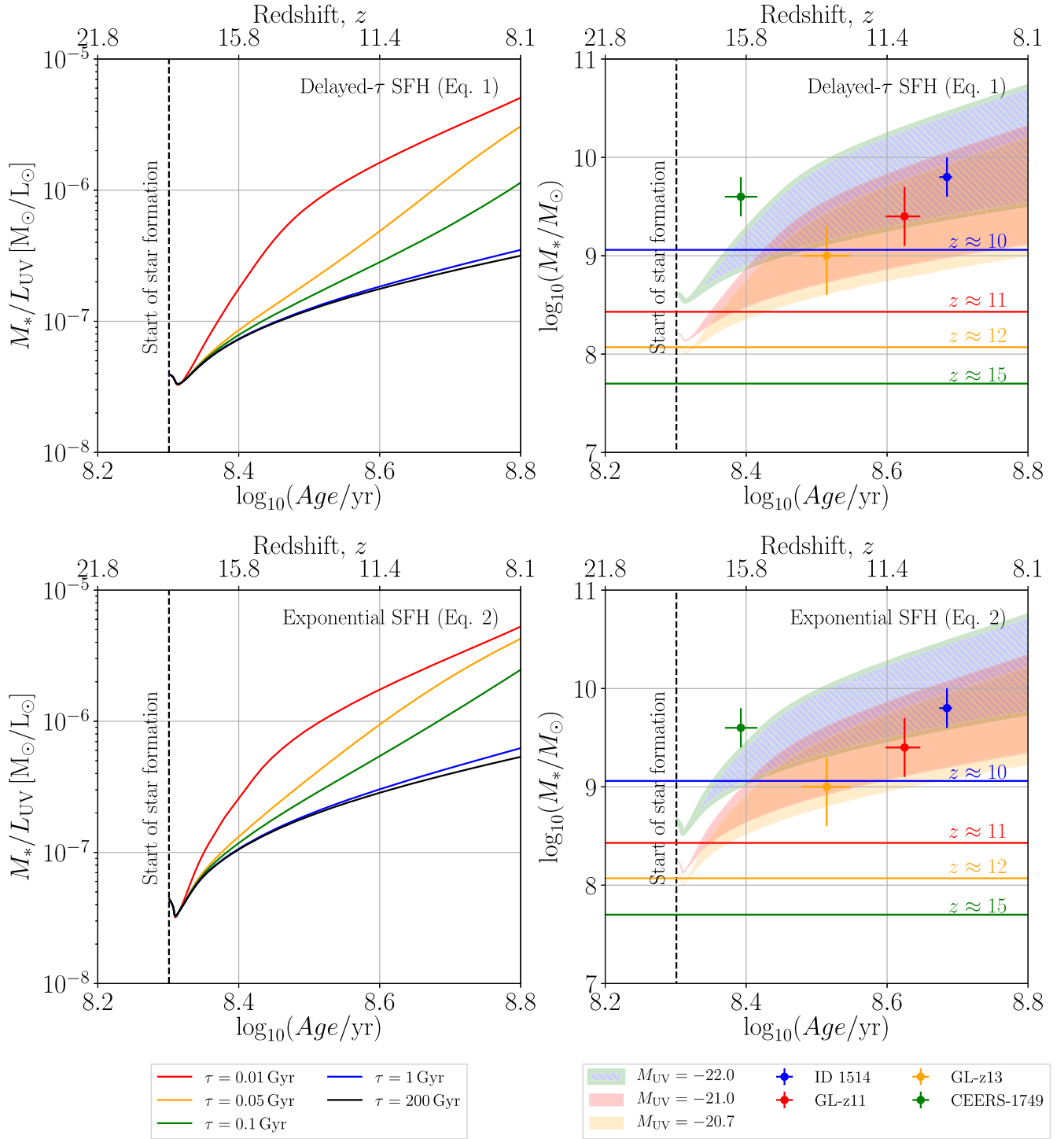


Figure 3. Left panels: cosmic time evolution of the stellar M_*/L_{UV} ratio for stellar populations constructed assuming an invariant canonical IMF and using a delayed- τ (Equation (1); top panels) and an exponentially increasing SFH (Equation (2); bottom panels). We assume that star formation starts 200 Myr after the Big Bang (dashed vertical line). The minimum mass-to-light ratio for these galaxies assuming different SFHs is $M_*/L_{UV} \approx 3.2 \times 10^{-8} M_\odot/L_\odot$. Right panels: cosmic time evolution of the total stellar mass of the galaxy candidates CEERS-1749 (green hatched area), GL-z13 (orange area), GL-z11 (red area), and ID 1514 (blue area) calculated based on the inferred mass-to-light ratios of the left panels. The colored areas cover the stellar mass range for SFHs with τ values between 0.01 Gyr (upper limit) and 200 Gyr (lower limit; see the left panels). The filled circles with error bars show the observed values as quantified by Adams et al. (2022), Naidu et al. (2022b), Naidu et al. (2022a). The most massive subhalos in terms of stellar mass in the Λ CDM simulations are shown as horizontal lines.

quantify how quickly galaxies form in the currently most advanced cosmological simulations. Using state-of-the-art Λ CDM simulations of the IllustrisTNG and EAGLE project, we showed that the stellar mass buildup is much more efficient in the early universe than predicted by these Λ CDM models (see also, e.g., Boylan-Kolchin 2022; Lovell et al. 2022). In

particular, the stellar masses of ID 1514 (Adams et al. 2022), ID 14924 (Labbe et al. 2022), GL-z11, GL-z13 (Naidu et al. 2022b), and CEERS-1749 (Naidu et al. 2022a) analyzed in Section 3 are higher by about 1 order of magnitude than the most massive galaxies formed in these simulations. In particular, massive high-redshift candidates appear more

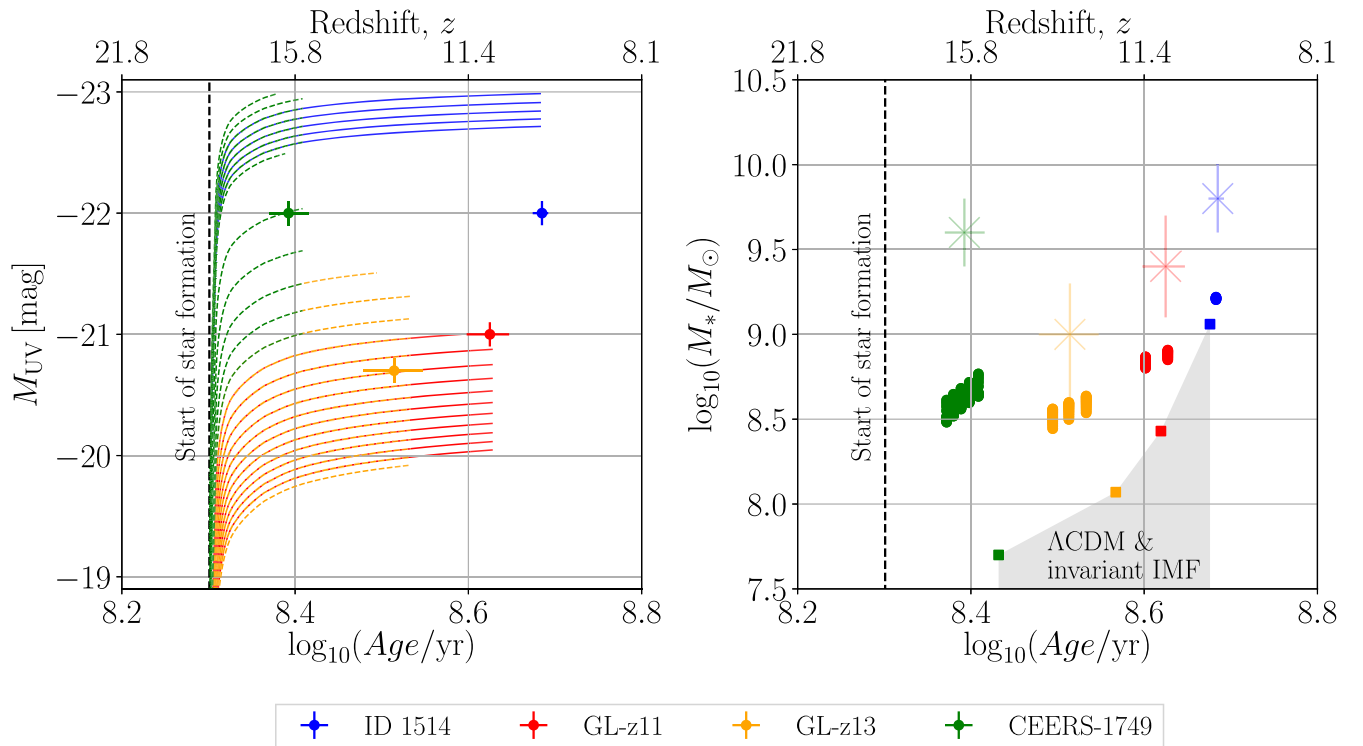


Figure 4. Left panel: cosmic time evolution of the absolute UV-band magnitude for stellar populations constructed using constant SFRs and assuming the IGIMF theory and that star formation starts 200 Myr after the Big Bang (dashed vertical line). The shown green, orange, red, and blue models match the observed magnitudes within ± 1 mag at the 1σ redshift interval of the galaxy candidates CEERS-1749, GL-z13, GL-z11, and ID 1514, respectively. The error bars show the observed absolute magnitudes of these four galaxy candidates. Right panel: the filled circles show the stellar masses of the galaxy candidates (of same color as the corresponding filled circles) assuming the M_*/L_{UV} ratios of the IGIMF models presented in the left panel. The faded error bars refer to the reported stellar masses as derived by Adams et al. (2022), Naidu et al. (2022b), Naidu et al. (2022a) based on an invariant canonical IMF. The squares mark the upper stellar mass limit found in the Λ CDM simulations assuming an invariant canonical IMF, and would be smaller for stronger-feedback regulation through an early top-heavy gwIMF.

frequent at $z \gtrsim 10$ than expected in the Λ CDM framework. For example, Boylan-Kolchin (2022) argued that a volume of $\approx 10^8 \text{ cMpc}^3$ is required to explain ID 14924 with $\log_{10}(M/M_{\odot}) = 10.93$ at $z = 9.92$ (Labbe et al. 2022). However, the survey covers $\approx 10^5 \text{ cMpc}^3$ at $z = 10 \pm 1$ (see Section 3 of Boylan-Kolchin 2022). The TNG100-1 and RefL 0100N1504 simulations have a box volume of $\approx 10^6 \text{ cMpc}^3$ suggesting that the absence of massive galaxies in these runs is not because of a too small simulation volume.

The discrepancy between the observed and simulated stellar mass buildup could be caused by several reasons. First of all, high photometric redshifts can emerge due to dust reddening. For example, Zavala et al. (2022) demonstrated that Lyman-break galaxy candidates at $z_{\text{phot}} \gtrsim 12$ can resemble dusty star-forming galaxies at $z \lesssim 6-7$. Second, it could be that the high observed stellar masses are caused by an erroneous calibration of JWST.

Furthermore, it has been argued that star formation could be much more efficient in the early universe (e.g., Naidu et al. 2022b; Harikane et al. 2022; Mason et al. 2022). Assuming that the Λ CDM model is the correct description of the universe, this would mean that the underlying galaxy formation and evolution interstellar medium models of the EAGLE and IllustrisTNG runs must be improved in order to reproduce such galaxies. For example, these simulations assume that gas above a given density threshold (e.g., Schaye et al. 2015; Nelson et al. 2019b) is able to form stars, which is likely a too simplified implementation especially for describing high-redshift galaxies. Boylan-Kolchin (2022) showed that even a 100% star

formation efficiency in Λ CDM would not be enough to explain the stellar mass density measured by Labbe et al. (2022).

Another possibility is that the IMF systematically varies with the galactic properties. The IllustrisTNG and EAGLE simulations and the analysis of the Sections 3 and 3.1 assume an invariant IMF, but it is expected that metal-poor star-forming stellar populations follow a top-heavy IMF. Using the IGIMF theory we calculated the gwIMF of the observed galaxy candidates in dependence of the metallicity and SFR of forming galaxies resulting in lower stellar masses compared to an invariant canonical IMF. For this, the IGIMF theory has to be included in cosmological simulations (see, e.g., Ploeckinger et al. 2014) in order to make a firm conclusion if a top-heavy IMF can resolve the reported tension.

Finally, the present findings can also imply that structure formation is much more efficient and/or that the observed universe is even older than predicted by Λ CDM. The existence of these massive galaxies $\approx 300-400$ Myr after the Big Bang also questions the hierarchical (bottom-up) structure formation suggesting that late-type galaxies begin to form early through the initial monolithic collapse of rotating post-Big-Bang gas clouds (Wittenburg et al. 2020) while early-type massive galaxies and associated formation of supermassive black halos form by the monolithic collapse of post-Big-Bang gas clouds with little net rotation (e.g., Kroupa et al. 2020b; Wittenburg et al. 2020; Yan et al. 2021; Eappen et al. 2022).

Evidence for an enhanced growth of structures has been reported at different astrophysical scales and redshift ranges in the observed universe. For example, Steinhardt et al. (2016) showed that the observed number density of luminous galaxies

at $5 \lesssim z \lesssim 10$ is much higher than predicted by the Λ CDM model (see their Figure 1). However, their analysis relies on the stellar-to-halo mass relation from Leauthaud et al. (2012) measured only at $z = 0.2 - 1$, while, e.g., Behroozi et al. (2019) suggest that there is a strong evolution at $z \gtrsim 5$. Furthermore, the existence of the massive interacting galaxy cluster El Gordo (ACT-CL J0102-4915; Marriage et al. 2011) at $z = 0.87$ and the Keenan–Barger–Cowie void (Keenan et al. 2013) at $z \lesssim 0.07$ both individually falsify the hierarchical Λ CDM structure formation with more than 5σ (Haslbauer et al. 2020; Asencio et al. 2021).

An enhanced growth of structure compared to the Λ CDM paradigm is expected in Milgromian dynamics (Milgrom 1983; Angus 2009; Malekjani et al. 2009; Famaey & McGaugh 2012; Kroupa et al. 2012; Haslbauer et al. 2020; Banik & Zhao 2022). Assuming the cosmic microwave background as the $z = 1100$ boundary condition and because of the reduced power on < 1 Mpc scales compared to Λ CDM (Angus & Diaferio 2011) due to the missing cold dark matter (CDM) component, it may be impossible to form galaxies in the early universe.


This work indicates that the currently available most advanced Λ CDM simulations cannot form galaxies as massive as observed at $z_{\text{phot}} \gtrsim 10$. This tension needs to be readdressed for extreme SFHs and/or if the gwIMF was top-heavy, which would reduce the stellar mass buildup through more intense feedback.

Upcoming ultradeep and wider-area JWST observations will reveal more light on the number density of such luminous high-redshift galaxies over redshift required to evaluate the significance of the here-reported tension of the stellar mass buildup of high-redshift galaxies in more detail.

We thank an anonymous referee for helpful comments that significantly improved the manuscript. This project was largely conducted at the Charles University in Prague and we acknowledge the “DAAD-Eastern-European” exchange program for financing visits at the Charles University in Prague during which we discussed several aspects of the formation and evolution of high-redshift galaxy candidates in the Λ CDM and Milgromian frameworks. We are also grateful to Nils Wittenburg, Nick Samaras, Ingo Thies, and Elena Asencio for helpful discussions on structure formation in Milgromian dynamics.

ORCID iDs

Moritz Haslbauer  <https://orcid.org/0000-0002-5101-6366>

Pavel Kroupa  <https://orcid.org/0000-0002-7301-3377>

Akram Hasani Zonoozi  <https://orcid.org/0000-0002-0322-9957>

Hosein Haghi  <https://orcid.org/0000-0002-9058-9677>

References

Adams, N. J., Conselice, C. J., Ferreira, L., et al. 2022, arXiv:2207.11217v2
 Angus, G. W. 2009, *MNRAS*, 394, 527
 Angus, G. W., & Diaferio, A. 2011, *MNRAS*, 417, 941
 Asencio, E., Banik, I., & Kroupa, P. 2021, *MNRAS*, 500, 5249

Atek, H., Shuntov, M., Furtak, L. J., et al. 2022, arXiv:2207.12338v1
 Banik, I., & Zhao, H. 2022, *Symm*, 14, 1331
 Behroozi, P., Wechsler, R. H., Hearin, A. P., & Conroy, C. 2019, *MNRAS*, 488, 3143
 Boyle-Kolchin, M. 2022, arXiv:2208.01611v1
 Carnall, A. C., Begley, R., McLeod, D. J., et al. 2022, *MNRAS*, Advance Access
 Crain, R. A., Schaye, J., Bower, R. G., et al. 2015, *MNRAS*, 450, 1937
 Eappen, R., Kroupa, P., Wittenburg, N., Haslbauer, M., & Famaey, B. 2022, *MNRAS*, 516, 1081
 Efstathiou, G., Sutherland, W. J., & Maddox, S. J. 1990, *Natur*, 348, 705
 Famaey, B., & McGaugh, S. S. 2012, *LRR*, 15, 10
 Furtak, L. J., Shuntov, M., Atek, H., et al. 2022, arXiv:2208.05473v1
 Harikane, Y., Ouchi, M., Oguri, M., et al. 2022, arXiv:2208.01612v1
 Haslbauer, M., Banik, I., & Kroupa, P. 2020, *MNRAS*, 499, 2845
 Jeřábková, T., Hasani Zonoozi, A., Kroupa, P., et al. 2018, *A&A*, 620, A39
 Keenan, R. C., Barger, A. J., & Cowie, L. L. 2013, *ApJ*, 775, 62
 Kroupa, P. 2001, *MNRAS*, 322, 231
 Kroupa, P., Haslbauer, M., Banik, I., Nagesh, S. T., & Pflamm-Altenburg, J. 2020a, *MNRAS*, 497, 37
 Kroupa, P., Pawłowski, M., & Milgrom, M. 2012, *IJMPD*, 21, 1230003
 Kroupa, P., Subr, L., Jerabkova, T., & Wang, L. 2020b, *MNRAS*, 498, 5652
 Kroupa, P., & Weidner, C. 2003, *ApJ*, 598, 1076
 Kroupa, P., Weidner, C., Pflamm-Altenburg, J., et al. 2013, in *Planets, Stars and Stellar Systems. Volume 5: Galactic Structure and Stellar Populations*, ed. T. D. Oswalt & G. Gilmore, Vol. 5 (Dordrecht: Springer), 115
 Labbe, I., van Dokkum, P., Nelson, E., et al. 2022, arXiv:2207.12446v2
 Leauthaud, A., Tinker, J., Bundy, K., et al. 2012, *ApJ*, 744, 159
 Lovell, C. C., Harrison, I., Harikane, Y., Tacchella, S., & Wilkins, S. M. 2022, arXiv:2208.10479v1
 Malekjani, M., Rahvar, S., & Haghi, H. 2009, *ApJ*, 694, 1220
 Marigo, P., & Girardi, L. 2007, *A&A*, 469, 239
 Marigo, P., Girardi, L., Bressan, A., et al. 2008, *A&A*, 482, 883
 Marinacci, F., Vogelsberger, M., Pakmor, R., et al. 2018, *MNRAS*, 480, 5113
 Marriage, T. A., Acquaviva, V., Ade, P. A. R., et al. 2011, *ApJ*, 737, 61
 Mason, C. A., Trenti, M., & Treu, T. 2022, arXiv:2207.14808v2
 McAlpine, S., Helly, J. C., Schaller, M., et al. 2016, *A&C*, 15, 72
 Milgrom, M. 1983, *ApJ*, 270, 365
 Naidu, R. P., Oesch, P. A., Setton, D. J., et al. 2022a, arXiv:2208.02794v1
 Naidu, R. P., Oesch, P. A., van Dokkum, P., et al. 2022b, arXiv:2207.09434v1
 Naiman, J. P., Pillepich, A., Springel, V., et al. 2018, *MNRAS*, 477, 1206
 Nelson, D., Pillepich, A., Springel, V., et al. 2018, *MNRAS*, 475, 624
 Nelson, D., Pillepich, A., Springel, V., et al. 2019a, *MNRAS*, 490, 3234
 Nelson, D., Springel, V., Pillepich, A., et al. 2019b, *ComAC*, 6, 2
 Oesch, P. A., Brammer, G., van Dokkum, P. G., et al. 2016, *ApJ*, 819, 129
 Ostriker, J. P., & Steinhardt, P. J. 1995, *Natur*, 377, 600
 Pillepich, A., Nelson, D., Hernquist, L., et al. 2018a, *MNRAS*, 475, 648
 Pillepich, A., Nelson, D., Springel, V., et al. 2019, *MNRAS*, 490, 3196
 Pillepich, A., Springel, V., Nelson, D., et al. 2018b, *MNRAS*, 473, 4077
 Planck Collaboration I. 2014, *A&A*, 571, A1
 Planck Collaboration XIII. 2016, *A&A*, 594, A13
 Ploechinger, S., Hensler, G., Recchi, S., Mitchell, N., & Kroupa, P. 2014, *MNRAS*, 437, 3980
 Rieke, M. J., Kelly, D., & Horner, S. 2005, *Proc. SPIE*, 5904, 1
 Schaye, J., Crain, R. A., Bower, R. G., et al. 2015, *MNRAS*, 446, 521
 Schneider, F. R. N., Sana, H., Evans, C. J., et al. 2018, *Sci*, 359, 69
 Senchyna, P., Stark, D. P., Charlot, S., et al. 2021, *MNRAS*, 503, 6112
 Springel, V. 2005, *MNRAS*, 364, 1105
 Springel, V. 2010, *MNRAS*, 401, 791
 Springel, V., Pakmor, R., Pillepich, A., et al. 2018, *MNRAS*, 475, 676
 Steinhardt, C. L., Capak, P., Masters, D., & Speagle, J. S. 2016, *ApJ*, 824, 21
 Weidner, C., & Kroupa, P. 2006, *MNRAS*, 365, 1333
 Wittenburg, N., Kroupa, P., & Famaey, B. 2020, *ApJ*, 890, 173
 Yan, H., Ma, Z., Ling, C., et al. 2022, arXiv:2207.11558v1
 Yan, Z., Jeřábková, T., & Kroupa, P. 2021, *A&A*, 655, A19
 Zavala, J. A., Buat, V., Casey, C. M., et al. 2022, arXiv:2208.01816v1
 Zhang, Z.-Y., Romano, D., Ivison, R. J., Papadopoulos, P. P., & Matteucci, F. 2018, *Natur*, 558, 260
 Zonoozi, A. H., Mahani, H., & Kroupa, P. 2019, *MNRAS*, 483, 46